



Short O–O separation in layered oxide Na_{0.67}CoO₂ enables an ultrafast oxygen evolution reaction

HPSTAR
878-2019

Hao Wang^{a,b,c,d,1}, Jinpeng Wu^{e,f,1}, Andrei Dolocan^{a,b}, Yutao Li^{a,b,2}, Xujie Lü^g, Nan Wu^{a,b}, Kyusung Park^{a,b}, Sen Xin^{a,b}, Ming Lei^{c,d}, Wanli Yang^e, and John B. Goodenough^{a,b,2}

^aMaterials Research Program, The University of Texas at Austin, Austin, TX 78712; ^bThe Texas Materials Institute, The University of Texas at Austin, Austin, TX 78712; ^cState Key Laboratory of Information Photonics and Optical Communications, Beijing University of Posts and Telecommunications, 100876 Beijing, China; ^dSchool of Science, Beijing University of Posts and Telecommunications, 100876 Beijing, China; ^eAdvanced Light Source, Lawrence Berkeley National Laboratory, Berkeley, CA 94720; ^fStanford Institute for Materials and Energy Sciences, Stanford Linear Accelerator Center (SLAC) National Accelerator Laboratory, Menlo Park, CA 94025; and ^gCenter for High Pressure Science and Technology Advanced Research, 201203 Shanghai, China

Contributed by John B. Goodenough, May 7, 2019 (sent for review January 18, 2019; reviewed by Peter Bruce and Jean-Marie Tarascon)

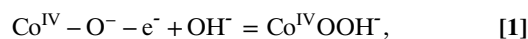
The layered oxide Na_{0.67}CoO₂ with Na⁺ occupying trigonal prismatic sites between CoO₂ layers exhibits a remarkably high room temperature oxygen evolution reaction (OER) activity in alkaline solution. The high activity is attributed to an unusually short O–O separation that favors formation of peroxide ions by O[–]–O[–] interactions followed by O₂ evolution in preference to the conventional route through surface O–OH[–] species. The dependence of the onset potential on the pH of the alkaline solution was found to be consistent with the loss of H⁺ ions from the surface oxygen to provide surface O[–] that may either be attacked by solution OH[–] or react with another O[–]; a short O–O separation favors the latter route. The role of a strong hybridization of the O–2p and low-spin Co^{III}/Co^{IV} π-bonding d states is also important; the OER on other Co^{III}/Co^{IV} oxides is compared with that on Na_{0.67}CoO₂ as well as that on IrO₂.

air electrodes | water electrolysis | catalytic mechanisms | structure–property relationship

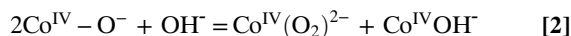
Highly active oxygen evolution reaction (OER) catalysts with a long-term stability are required to reduce the energy loss, increase the rate performance, and improve the cycling stability of different energy conversion and storage systems, particularly in electrochemical water electrolysis and rechargeable metal–air aqueous electrolyte batteries (1–4). The most active OER catalyst, IrO₂, is expensive and shows a high overpotential of 0.3 V at 10 mA·cm^{–2}; moreover, it is unstable at the applied potential in an alkaline electrolyte, which degrades its activity and limits its application (5–7).

Low-cost transition metal (TM) oxides are promising candidates for OER catalysts (8–17). AMO₃ perovskites with controllable chemical compositions and electronic structures by substituting the cations on A and M sites have been extensively investigated as OER catalysts (18–22). Some perovskite oxides (e.g., Ba_{0.5}Sr_{0.5}Co_{0.8}Fe_{0.2}O_{3–8}, Hg₂Ru₂O₇, and CaCu₃Fe₄O₁₂) exhibit comparable or even better OER catalytic activity than that of IrO₂ (3, 5, 23). However, the obtained OER descriptor of $e_g \approx 1$ on the d-orbital manifold of Mⁿ⁺ ions in AMO₃ perovskites for their excellent OER activity is challenged by the good OER on 4d/5d TM oxide catalysts with zero antibonding e_g electrons such as IrO₂ and Hg₂Ru₂O₇ (24–27). In addition to the OER activity, the stability and the preparation condition of the catalysts are 2 other critical parameters for their large-scale application. For example, the crystalline Ba_{0.5}Sr_{0.5}Co_{0.8}Fe_{0.2}O_{3–8} phase becomes amorphous after OER testing in an alkaline electrolyte, and the stable Hg₂Ru₂O₇ and CaCu₃Fe₄O₁₂ catalysts with high valence Ru⁵⁺ and Fe⁴⁺ ions can only be prepared at an extremely high pressure of 6 and 15 GPa, respectively (23). The instability of TM oxides originates from cations that can dissolve into the alkaline solution and from lattice oxygen loss during the OER (28). Increasing the Mⁿ⁺–O^{2–} bond strength of oxides helps to improve their stability. Therefore, developing an easily prepared, efficient, and durable OER catalyst based on Earth-abundant elements is still a challenge.

We have recently studied the onset potentials and OER activities of 2 cubic perovskites, CaCoO₃ and SrCoO₃, prepared under high pressure (29); both have Co^{IV} ions having similar intermediate spin states t^4e^* , but CaCoO₃ had a significantly shorter Co^{IV}–O bond (1.87 Å) and showed a higher OER activity than SrCoO₃ as a result of its reduced lattice parameter. After surface deprotonation at a charging potential $V_{\text{ch}} = V_{\text{on}}$, where V_{on} was the onset potential, the surface Co^{IV}–O[–] were attacked by solution OH[–],



but the competitive reaction



followed by



was much stronger on CaCoO₃ because of its much smaller lattice parameter, which reduced the surface O–O separation. The O[–] + O[–] = (O₂)^{2–} reaction is faster the shorter the O–O separation of the catalyst. In the conventional reaction route, the O[–] ion is attacked by a solution OH[–] to form OOH[–], and the OOH[–] + OH[–] = (O₂)^{2–} + H₂O; this mechanism is independent of the O–O separation.

These findings recommended to us a search for stable oxides with a shorter surface oxygen separation that can be prepared at

Significance

The development of a low-cost, stable, and more active electrocatalyst for the oxygen evolution reaction (OER) is critical for the practical storage of electric power in hydrogen gas produced by the electrolysis of water. We demonstrate a stable OER of higher rate at a lower voltage with a low-cost oxide that provides, as an alternative to the conventional reaction route, a faster route that is greatly enhanced by an unusually short O–O separation.

Author contributions: Y.L. and J.B.G. conceived the idea and designed research; H.W., A.D., Y.L., X.L., N.W., M.L., and W.Y. performed research; H.W., J.W., A.D., Y.L., K.P., and S.X. analyzed data; Y.L. and J.B.G. wrote the paper; J.W. and W.Y. performed the sXAS and mRIXS characterization; A.D. performed the time-of-flight secondary ion mass spectrometry (TOF-SIMS); and X.L. did the synchrotron experiment.

Reviewers: P.B., University of St. Andrews; and J.-M.T., Collège de France.

The authors declare no competing interest.

Published under the [PNAS license](#).

¹H.W. and J.W. contributed equally to this work.

²To whom correspondence may be addressed. Email: lyttu@utexas.edu or jgoodenough@mail.utexas.edu.

This article contains supporting information online at www.pnas.org/lookup/suppl/doi:10.1073/pnas.1901046116/-DCSupplemental.

ambient pressure. Therefore, we prepared a metallic layered oxide $\text{Na}_{0.67}\text{CoO}_2$ with low-spin $\text{Co}^{\text{III/IV}}$ ions (Co^{III} : $\pi^*6\sigma^*0$; Co^{IV} : $\pi^*5\sigma^*0$) and a much shorter O–O separation than on CaCoO_3 to study further the influence of zeta potential, surface oxygen separation, and the pH of the aqueous medium on the onset potential and OER activity. Metallic, low-spin $\text{Na}_{0.67}\text{CoO}_2$ has a strong $\text{Co}^{\text{III/IV}}\text{--O}$ interaction as a result of empty σ -antibond e_g orbitals and itinerant π -bonding electrons, which reduces the charge transfer resistance during the OER; $\text{Na}_{0.67}\text{CoO}_2$ has a zero zeta potential at pH = 4 and shows a pH-dependent onset potential for the OER consistent with the potential for the $\text{CoOH}^- - e^- + \text{OH}^- = \text{CoO}^- + \text{H}_2\text{O}$ reaction.

Results

The Crystal and Electronic Structure of $\text{Na}_{0.67}\text{CoO}_2$. Synchrotron powder X-ray diffraction (XRD) and powder X-ray diffraction patterns of as-prepared $\text{Na}_{0.67}\text{CoO}_2$ (Fig. 1 and *SI Appendix, Fig. S1*) confirm the layered structure of $\text{Na}_{0.67}\text{CoO}_2$. Two-dimensional CoO_2 layers with edge-sharing CoO_6 octahedra in trigonal $\text{Na}_{0.67}\text{CoO}_2$ (space group: R-3c) are separated by sodium layers. The Na^+ occupy 3 different trigonal prismatic sites, Na1 and Na2 (Na2a and Na2b) in *SI Appendix, Table S1*; each shares 6 edges and 2 triangular faces along the c axis with the CoO_6 octahedra vertically above and below. The Na1 ions are energetically less favorable because of the coulombic repulsions from 2 Co ions in face-sharing octahedra. The Co ions of $\text{Na}_{0.67}\text{CoO}_2$ have 4 different positions; the distorted CoO_6 octahedra have a similar average Co–O bond distance, but one shortest O–O separation (2.30 Å; Fig. 1F) than that of cubic CaCoO_3 (O–O: 2.64 Å) in which the Co^{IV} have an intermediate spin state ($t^4\sigma^*1$). About 0.3 wt%

Co_3O_4 impurity was found to exist in the sample by refining the synchrotron data. The $\text{Na}_{0.67}\text{CoO}_2$ sample had an average particle size of 15 μm (*SI Appendix, Fig. S3*), and the energy dispersive spectroscopy (EDS) mapping revealed a uniform distribution of Na, Co, and O elements.

The electronic conductivity and magnetic properties of $\text{Na}_{0.67}\text{CoO}_2$ were investigated to determine the d -electron configuration of the $\text{Co}^{\text{III/IV}}$ ions (Fig. 1D). The temperature dependence of resistivity of $\text{Na}_{0.67}\text{CoO}_2$ shows a metallic behavior down to 2 K, with a large residual resistance ratio; a nonlinear magnetic susceptibility curve from 2 to 300 K is also consistent with itinerant d electrons. A spin-polarized first-principle calculation was performed, and the density of states of Co ions from $\text{Na}_{0.67}\text{CoO}_2$ is shown in Fig. 1E. The conduction band of $\text{Na}_{0.67}\text{CoO}_2$, which contains one spin component of t_{2g} orbitals, is not full, indicating a metallic conductivity of $\text{Na}_{0.67}\text{CoO}_2$. The higher electronic conductivity of $\text{Na}_{0.67}\text{CoO}_2$ reduces the charge transfer resistance (R_{ct}) and the ohmic potential drop of the OER; the R_{ct} of $\text{Na}_{0.67}\text{CoO}_2$ is one order of magnitude smaller than that of the electronic insulator Co_3O_4 , which is above 1.6 V (*SI Appendix, Fig. S4*).

Soft X-ray absorption spectroscopy (sXAS), which is quite sensitive to the TM $3d$ states because of the strong dipole-allowed $2p\text{--}3d$ (L edge) excitations (30–33), was performed to explore the valence and spin states of the Co ions of $\text{Na}_{0.67}\text{CoO}_2$ (Fig. 2). With a probe depth of 10 nm, the total electron yield (TEY) mode of sXAS is quite an effective surface-sensitive probe, as shown in Fig. 2A and B. Due to the core-hole spin-orbit coupling, the Co L edge in Fig. 2A is well separated into 2 branches, that is, L_3 (between 774 and 787 eV) and L_2 (between 788 and 799 eV). The branching ratio of the L_3 and L_2 edges, which is greatly affected by

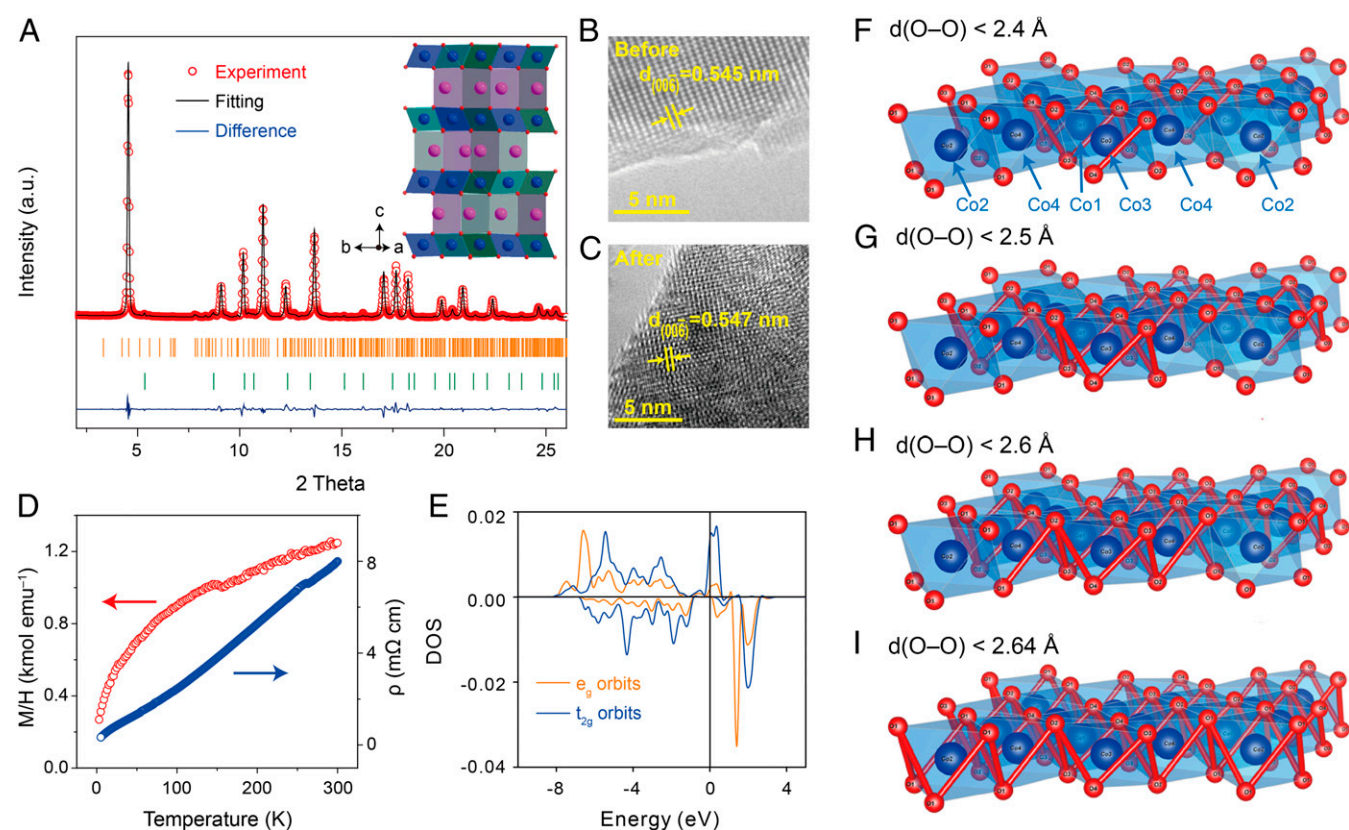


Fig. 1. Crystal structure and magnetic and transport properties of $\text{Na}_{0.67}\text{CoO}_2$. (A) Observed, calculated patterns, and their difference for the Rietveld refinement of the synchrotron XRD of $\text{Na}_{0.67}\text{CoO}_2$; (Inset) its crystal structure (pink, Na; blue, Co; red, O). (B and C) TEM images of $\text{Na}_{0.67}\text{CoO}_2$ before and after OER measurements. (D) Temperature dependence of resistivity and magnetization. (E) Electronic spin states of Co^{IV} ions and schematic band diagrams of $\text{Na}_{0.67}\text{CoO}_2$. (F–I) The O–O bonds shorter than (2.4 to 2.64) Å are highlighted with thick red lines.

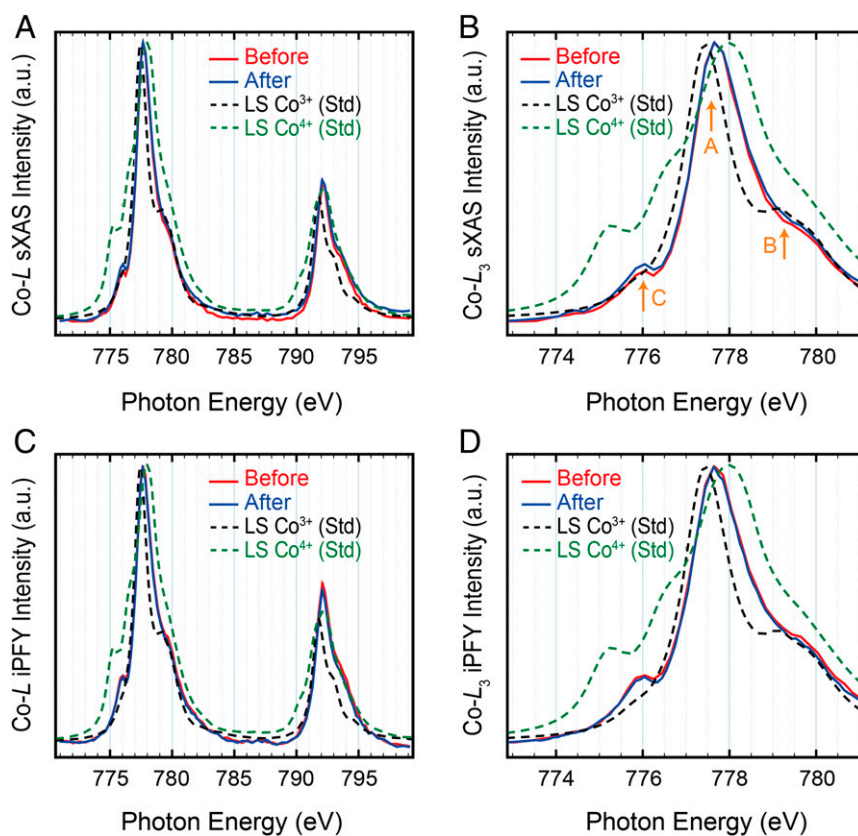


Fig. 2. The absorption profiles of Co^{III} and Co^{IV} in $\text{Na}_{0.67}\text{CoO}_2$ probed by sXAS and mRIXS. (A and B) The sXAS TEY of (A) Co L edge and (B) magnified L_3 edge obtained with a surface probe having a probe depth of 10 nm. (C and D) The mRIXS iPFY of (C) Co L edge and (D) magnified L_3 edge by a bulk probe with a probe depth of 100 nm.

the spin-orbit coupling and especially by the $2p$ - $3d$ multiplet effects, can be utilized to deduce the spin state of Co (34, 35). Quantitatively, for the statistical ratio of the integrated intensity of 2 edges, namely $I_{L_3}/(I_{L_3} + I_{L_2})$, the high-spin state has a higher one than the low-spin state. Respectively for the samples before and after catalysis reaction, the statistical branching ratio of the Co L inverse partial fluorescence yield (iPFY) is 0.689 ± 0.005 and 0.686 ± 0.005 . Based on the atomic multiplet calculations (36, 37), the standard spectra of LS Co within the octahedral (CoO_6) structure is achieved as shown by dashed lines in Fig. 2 A and B, and that of HS is done as shown in *SI Appendix*, Fig. S6. While the calculated spectrum of LS Co (either Co^{3+} or Co^{4+}) has a branching ratio of 0.698 ± 0.005 , very close to the experimental Co L iPFY, that of HS has a much higher one of 0.780 ± 0.005 , suggesting that $\text{Na}_{0.67}\text{CoO}_2$ has a low-spin state (Co^{III} : t^6e^0 , Co^{IV} : t^5e^0). The density of states of Co ions from $\text{Na}_{0.67}\text{CoO}_2$, which is shown in Fig. 1E, also indicates low-spin $\text{Co}^{\text{III/IV}}$ ions. The valence state of the Co ions can be inferred by the Co L_3 peak position. As shown in Fig. 2B, the peak A located at 777.6 eV, which is 0.2 eV from the standard Co^{3+} (777.4 eV) and 0.4 eV from the standard Co^{4+} (778.0 eV). This position indicates that the valence of the Co ions is about 3.3+, consistent with the expected stoichiometry as prepared.

In addition, we demonstrate the bulk information as a supplement. Resulting from the self-absorption and saturation effects (38, 39), the bulk probe of sXAS, that is, total fluorescence yield mode with a probe depth of 100 nm (40), provided a noisy lineshape and an unreliable L_2/L_3 intensity ratio as shown in *SI Appendix*, Fig. S5. The iPFY is theoretically an undistorted absorption profile that can be extracted from the map of resonant inelastic X-ray scattering (mRIXS). In this work, we performed the Co L mRIXS measurement on $\text{Na}_{0.67}\text{CoO}_2$, and achieved the iPFY for characterizing the bulk Co status. (For the convenience

of the reader, we introduce how to extract the Co L iPFY from the mRIXS in *SI Appendix*, Fig. S5.) As shown in Fig. 2 C and D, the Co L iPFY spectra demonstrate a consistent lineshape with the TEY spectra, indicating that Co ions in the bulk of $\text{Na}_{0.67}\text{CoO}_2$ present the same low-spin electronic and 3.3+ valence state as those on the surface.

The OER Activity of $\text{Na}_{0.67}\text{CoO}_2$. The OER performance of $\text{Na}_{0.67}\text{CoO}_2$ was compared with that of rutile IrO_2 , spinel Co_3O_4 , and layered $\text{Co}(\text{OH})_2$ (Fig. 3). The current densities of all of the samples were normalized to the electrochemically active surface area to exclude geometric effects (*SI Appendix*, Fig. S7 and Table S2). The catalysts with different particle size have similar OER activities when the current density is normalized to the electrochemical surface area or the surface area confirmed by Brunauer-Emmett-Teller measurement (41). $\text{Na}_{0.67}\text{CoO}_2$ with an onset potential of 1.5 V vs. a reversible hydrogen electrode (RHE) had the smallest overpotential (0.29 V) at 10 mA cm^{-2} and the highest current density at voltages above 1.6 V; the layered $\text{Co}(\text{OH})_2$ and spinel Co_3O_4 exhibited a negligible catalytic current density compared with $\text{Na}_{0.67}\text{CoO}_2$. The smallest Tafel slope of 39 $\text{mV} \cdot \text{dec}^{-1}$ (Fig. 3C) for $\text{Na}_{0.67}\text{CoO}_2$ also indicates its excellent OER kinetics. The layered $\text{Li}_{1-x}\text{CoO}_2$ has a structure and $\text{Co}^{\text{III/IV}}\text{-O}$ bond similar to that in $\text{Na}_{0.67}\text{CoO}_2$, but the Li^+ are in octahedral sites and no O-O separation is reduced; it has a much higher onset potential and a smaller OER current density than $\text{Na}_{0.67}\text{CoO}_2$ (6).

The Surface Charge Density of $\text{Na}_{0.67}\text{CoO}_2$. The mean surface charge density of $\text{Na}_{0.67}\text{CoO}_2$ (Fig. 4A) was evaluated by its zeta potential in water with different pH. $\text{Na}_{0.67}\text{CoO}_2$ has a zero zeta potential at pH = 4; the strong covalence of the $\text{Co}^{\text{III/IV}}\text{-O}$ bond of $\text{Na}_{0.67}\text{CoO}_2$ makes it more acidic than the spinel Co_3O_4 , which

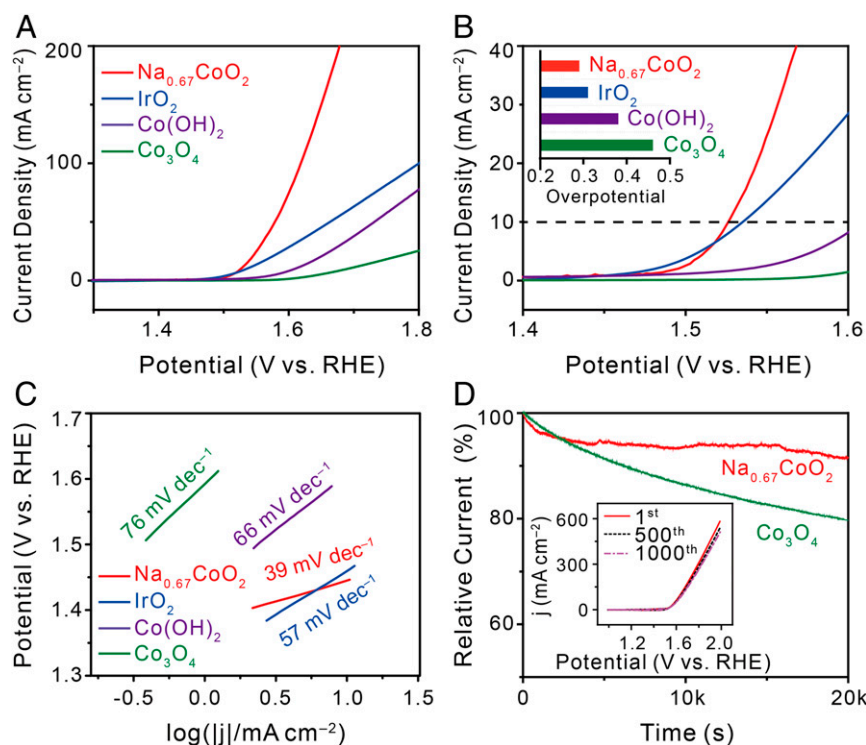


Fig. 3. OER performance of $\text{Na}_{0.67}\text{CoO}_2$, IrO_2 , $\text{Co}(\text{OH})_2$, and Co_3O_4 . (A) Linear sweep voltammograms at 1,600 revolutions per minute. in 0.1 M KOH. (B) The overpotential at 10 mA cm^{-2} (dashed line). (C) Tafel plots. (D) The chronoamperometric curves in an O_2 -saturated 0.1 M KOH electrolyte at 1.6 V vs. RHE and the CV curves of first, 500th, and 1,000th cycles (*Inset*).

has a weaker $\text{Co}^{\text{III}}\text{--O}$ bond and a high zero-zeta potential at $\text{pH} = 7.5$. IrO_2 with a strong $\text{Ir}^{\text{IV}}\text{--O}$ bond has a similar zeta potential curve to that of $\text{Na}_{0.67}\text{CoO}_2$, indicating analogous acidity of the surface states and pH influence on their OER.

The onset potential and activity of $\text{Na}_{0.67}\text{CoO}_2$ at different pH are compared with those of Co_3O_4 , $\text{Co}(\text{OH})_2$ and IrO_2 in Fig. 4 and *SI Appendix, Fig. S8*. The oxidation voltage of surface Co^{III} to Co^{IV} and the onset potential of $\text{Na}_{0.67}\text{CoO}_2$ were reduced with increasing pH (Fig. 4B) because of the easier deprotonation process at higher pH; the activities of $\text{Na}_{0.67}\text{CoO}_2$ and IrO_2 show a similar pH-dependent behavior on the RHE scale, and their OER currents increase significantly at high pH; however, both Co_3O_4 and $\text{Co}(\text{OH})_2$ have no significant OER current increase. The slope of all CV curves of these catalysts at voltages above 1.6 V increases exponentially with pH (Fig. 4D), and the most active $\text{Na}_{0.67}\text{CoO}_2$ has the biggest slope of all of the catalysts at different pH. Both $\text{Na}_{0.67}\text{CoO}_2$ and IrO_2 have a much larger slope change than Co_3O_4 and $\text{Co}(\text{OH})_2$, indicating different OER mechanisms in these catalysts.

The OER Stability of $\text{Na}_{0.67}\text{CoO}_2$. $\text{Na}_{0.67}\text{CoO}_2$ shows an excellent OER stability in an O_2 -saturated electrolyte with $\text{pH} = 13$ (Fig. 3D). More than 90% of its initial current density after 20,000 s was retained; and, after 1,000 cyclic voltammetry (CV) cycles, $\text{Na}_{0.67}\text{CoO}_2$ showed almost the same OER activity. The transmission electron microscopy (TEM) image (Fig. 1C) and XRD (*SI Appendix, Fig. S1*) results confirmed the same crystalline structure of bulk and surface $\text{Na}_{0.67}\text{CoO}_2$ before and after OER testing. The X-ray photoelectron spectroscopy (XPS) spectra of fresh $\text{Na}_{0.67}\text{CoO}_2$, $\text{Na}_{0.67}\text{CoO}_2$ soaked in KOH for a week, and $\text{Na}_{0.67}\text{CoO}_2$ after 1,000 CV cycles are shown in *SI Appendix, Fig. S9*; the Na, Co, and O peaks of $\text{Na}_{0.67}\text{CoO}_2$ after cycling are much weaker because of the covering Nafion binder on the particle surface; all of these XPS peaks retain the same positions, verifying the good stability of $\text{Na}_{0.67}\text{CoO}_2$ during OER. $\text{Na}_{0.67}\text{CoO}_2$ shows a stable peak position in sXAS, and the valence state of Co sXAS remains unchanged in the $\text{Na}_{0.67}\text{CoO}_2$ powder before

and after OER (Fig. 2). The strong Co–O bonds of $\text{Na}_{0.67}\text{CoO}_2$ increase its stability in alkaline solution.

The Surface of $\text{Na}_{0.67}\text{CoO}_2$ after OER. Because surface oxygens of $\text{Na}_{0.67}\text{CoO}_2$ participate in the OER, bulk lattice oxygen can diffuse to the surface oxygen vacancies after O_2 gas release and capture a proton from solution before the solution OH^- enters, and then the vacancies will be generated on these oxygens. The Co and O ions of a minimum 14-nm-thick surface of perovskite SrCoO_{3-x} have been reported to participate in the OER (42).

Time-of-flight secondary ion mass spectrometry (TOF-SIMS), which is an ultrahigh elemental and surface sensitive technique, was employed to study whether any chemical composition change occurs on the surface of $\text{Na}_{0.67}\text{CoO}_2$ before and after OER testing. Given the destructive nature of TOF-SIMS, all ionized fragments detected imply chemical bonding between the fragment elements prior to sputtering (43). TOF-SIMS depth profiling and high-resolution mapping were used to show the presence of CoOH and CoO_2H on the surface of the $\text{Na}_{0.67}\text{CoO}_2$ particles following OER (Fig. 5 and *SI Appendix, Fig. S10*). Due to the naturally high surface corrugation of $\text{Na}_{0.67}\text{CoO}_2$, both CoOH^- and CoO_2H^- secondary ion depth profiles were normalized by the corresponding Co^- profile in each sample to account for the topography changes between the $\text{Na}_{0.67}\text{CoO}_2$ surfaces before and after OER. As a proxy for bulk $\text{Na}_{0.67}\text{CoO}_2$, the Co^- signal was selected for normalization. Finally, we used the ratio between the Co^- -normalized CoOH^- and CoO_2H^- profiles before and after OER to demonstrate their surface localization after the OER in a ~ 70 -nm layer; the peak position of this ratio in Fig. 5A and B provided the localization. In comparison, the CoO^-/Co^- profile appears less enhanced at the surface, which suggests the OER produces only a limited amount of CoO at the $\text{Na}_{0.67}\text{CoO}_2$ surface (Fig. 5C). However, given the natural fragmentation of $\text{Na}_{0.67}\text{CoO}_2$ upon sputtering, the CoO^- signal could also be used as a marker for the bulk $\text{Na}_{0.67}\text{CoO}_2$. As such, TOF-SIMS high-resolution mapping of

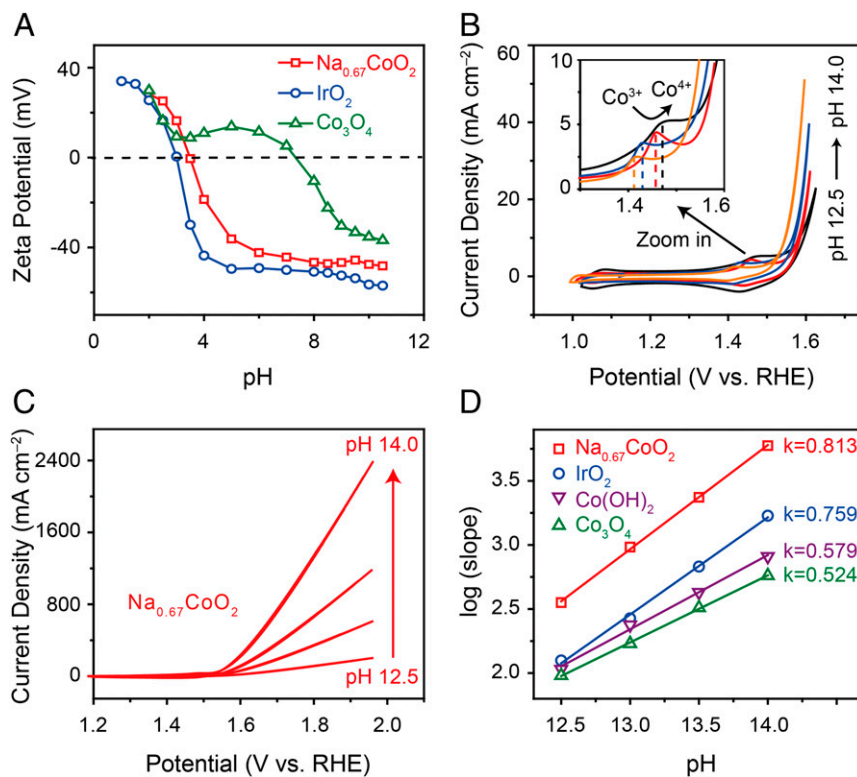
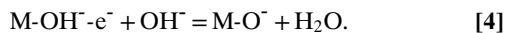


Fig. 4. The pH-dependent OER behavior of $\text{Na}_{0.67}\text{CoO}_2$. (A) Zeta potential of the catalysts. (B and C) CV measurements of $\text{Na}_{0.67}\text{CoO}_2$ in O_2 -saturated KOH with pH 12.5 to 14. Inset shows the enlarged CV part from 1.3 to 1.6 V. (D) The slope change of the linear CV curves at voltages above 1.7 V in B and C and *SI Appendix, Fig. S8* with different pH.

CoO^- and CoOH^- secondary ion fragments was performed to show directly the formation of CoOH at the surface of $\text{Na}_{0.67}\text{CoO}_2$ (Fig. 5D). Indeed, deep sputtering of the $\text{Na}_{0.67}\text{CoO}_2$ particles confirms the continuous presence of CoOH at their surface, as presented in Fig. 5D in the dual color overlay as a function of depth, that is, of Cs^+ sputtering time. The Na/Co ratio of $\text{Na}_{0.67}\text{CoO}_2$ was confirmed, by inductively coupled plasma mass spectrometry, not to change from before to after OER testing (*SI Appendix, Table S3*).

Discussion

In air, an exposed surface cation M of an oxide, especially one with a strong octahedral site preference energy, attracts water to complete its oxygen coordination; the hydrogen atoms of the adsorbed water H_2O are dispersed over the surface oxygen to create surface M-OH^- . In alkaline solution, an exposed surface cation attracts solution OH^- when it is oxidized during charge. Continuing removal of electrons from the oxide during charge in KOH solution induces the reaction (Fig. 6A)



This reaction occurs at a critical potential $V_c \leq V_{\text{on}}$, where V_{on} is the onset potential for the OER to occur with continuing charge; the resulting MO^- may be attacked by the solution OH^- ,

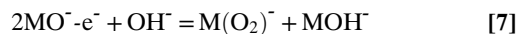


and the subsequent OER activity then depends on the relative rates of removal of the H^+ ,



and displacement of the O_2H^- by a solution OH^- . An O_2H^- can be an unwanted by-product of reaction 5.

Alternatively, 2 neighboring surface O^- may react with one another (Fig. 6B),



followed by



The rate of reaction 7 competes with that of reaction 5; it increases strongly with decreasing surface O–O separation. Therefore, the activity of the OER above the onset potential depends strongly on the surface O–O separation. The observation of an ultrafast OER in $\text{Na}_{0.67}\text{CoO}_2$ with an unusually short O–O separation demonstrates this dependence. A layer oxide Na_xCoO_2 with $x = 0.52, 0.65, \text{ and } 0.75$ has a different crystal structure (space group: P63/mmc) with our $\text{Na}_{0.67}\text{CoO}_2$ (R-3c); all of these 3 materials show almost the same OER activity after cycling. Our $\text{Na}_{0.67}\text{CoO}_2$ shows a much higher OER activity than the reported Na_xCoO_2 ; the overpotential at $10 \text{ mA}\cdot\text{cm}^{-2}$ of our $\text{Na}_{0.67}\text{CoO}_2$ is 0.29 V, which is much smaller than their Na_xCoO_2 (0.45 to 0.47 V) (44). In Na_xCoO_2 with space group P63/mmc, for example, $\text{Na}_{0.65}\text{CoO}_2$, Na and Co ions occupy 2 and 1 different positions, respectively; however, there are 3 Na and 4 Co positions in $\text{Na}_{0.67}\text{CoO}_2$ with space group R-3c. The O–O separation in $\text{Na}_{0.65}\text{CoO}_2$ is 2.57 Å, while the O–O separation of our $\text{Na}_{0.67}\text{CoO}_2$ is much smaller (the shortest O–O is 2.30 Å); the large O–O separation difference is caused by the different crystal structure and Na ordering. Their results also well support our conclusion that short O–O separation determines the OER activity. The relationship between the catalytic performance and the O–O bond length in Na_xCoO_2 and Li_xCoO_2 with different Na^+ and Li^+ proportion according to the previous report is shown

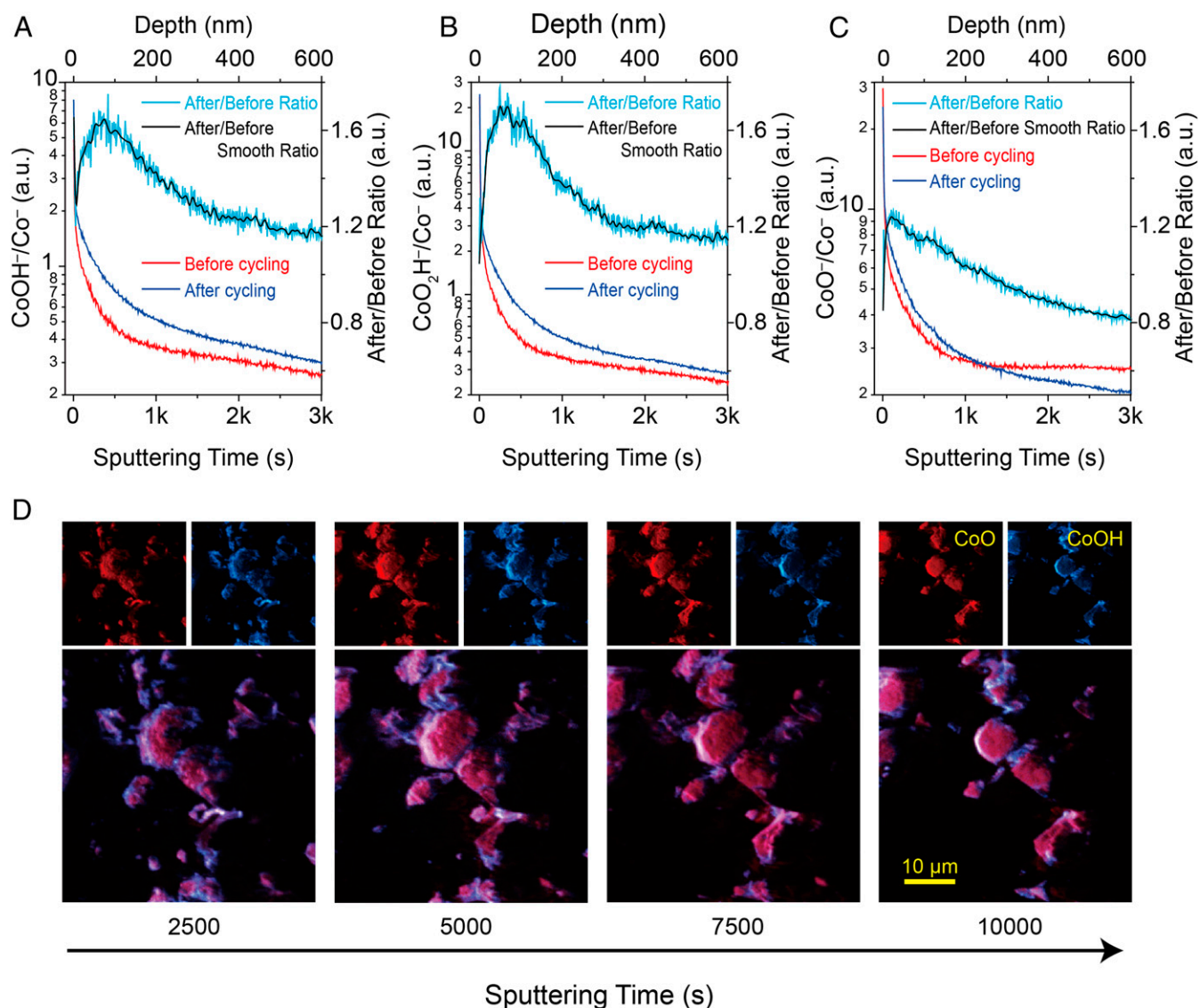


Fig. 5. TOF-SIMS depth profiling and high-resolution mapping of $\text{Na}_{0.67}\text{CoO}_2$ particles before and after OER. (A–C) TOF-SIMS depth profiling of $\text{Na}_{0.67}\text{CoO}_2$ before and after cycling. The intermediates CoOH^- , CoO_2H^- , and CoO^- increase after cycling. (D) Dual color overlays of high-resolution maps of the CoO^- and CoOH^- secondary ion signals demonstrating that CoOH^- mainly exists on the surface of the catalyst particles.

in *SI Appendix, Fig. S2*. The shorter the O–O bond length in these oxides, the smaller the overpotentials at $5 \text{ mA}\cdot\text{cm}^{-2}$, which confirms the key role of the short O–O separation in the OER performance of the $\text{Na}_{0.67}\text{CoO}_2$.

Reaction 4, which sets the onset potential, depends on the zeta potential of the oxide and the pH of the solution. Reaction 4 is favored the higher the pH of the solution and the greater the acidity of the oxide. The stronger the M–O bond, the more acidic is the oxide. The existence of itinerant electrons in π -bonding orbitals of d -wave symmetry not only lowers the resistance to the OER, but also testifies to a strong O-2p hybridization in the π -bonding as well as σ -bonding orbitals of d -wave symmetry.

Summary

The excellent OER activity of $\text{Na}_{0.67}\text{CoO}_2$ is the result of a short O–O separation that increases the rate of reaction 7 relative to reaction 5 and demonstrates the superior rate capability of reaction 7. The stability of the catalyst is the result of strong Co–O σ -bonding with the Co^{IV} configuration on $\pi^*5\sigma^*0$.

Materials and Methods

$\text{Na}_{0.67}\text{CoO}_2$ was prepared by a typical solid-state reaction with analytical grade Na_2CO_3 and Co_3O_4 as raw materials. First of all, the mixture of Na_2CO_3

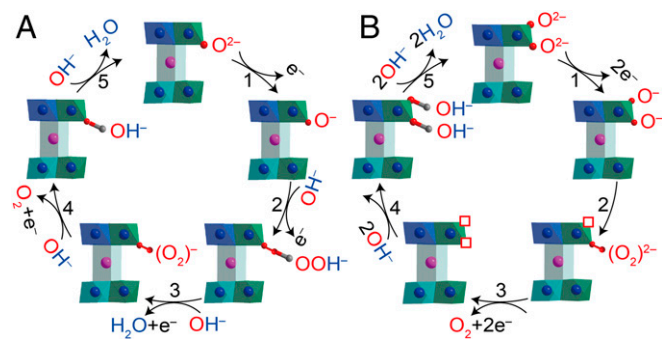


Fig. 6. Competing OER mechanisms on $\text{Na}_{0.67}\text{CoO}_2$. OER mechanism with surface lattice oxygen activated for OER to form peroxide either (A) in a CoO_2 layer or (B) between 2 neighboring CoO_2 layers.

and Co_3O_4 in a stoichiometric ratio with an excess of 5 mol% Na_2CO_3 was thoroughly ground in agate bowls, pressed into pellets, and sintered at 700 °C for 2 d, 900 °C for 15 h, and 950 °C for 10 h at a heating rate of 3 °C·min⁻¹ with intermediate grinding. These pellets, after sintering, were crushed and powdered to obtain a fine particle size. For comparison, commercial IrO_2 , $\text{Co}(\text{OH})_2$, and Co_3O_4 were purchased from Alfa Aesar and used without further purification.

ACKNOWLEDGMENTS. H.W. thanks the China Scholarship Council for the opportunity to work in Texas. This work was supported by the

- D. Chen, C. Chen, Z. M. Baiyee, Z. Shao, F. Ciucci, Nonstoichiometric oxides as low-cost and highly-efficient oxygen reduction/evolution catalysts for low-temperature electrochemical devices. *Chem. Rev.* **115**, 9869–9921 (2015).
- Y. Jiao, Y. Zheng, M. Jaroniec, S. Z. Qiao, Design of electrocatalysts for oxygen- and hydrogen-involving energy conversion reactions. *Chem. Soc. Rev.* **44**, 2060–2086 (2015).
- J. Suntivich, K. J. May, H. A. Gasteiger, J. B. Goodenough, Y. Shao-Horn, A perovskite oxide optimized for oxygen evolution catalysis from molecular orbital principles. *Science* **334**, 1383–1385 (2011).
- J. B. Goodenough, R. Manoharan, M. Paranthaman, Surface protonation and electrochemical activity of oxides in aqueous solution. *J. Am. Chem. Soc.* **112**, 2076–2082 (1990).
- J. T. Mefford *et al.*, Water electrolysis on $\text{La}_{1-x}\text{Sr}_x\text{CoO}_{3-\delta}$ perovskite electrocatalysts. *Nat. Commun.* **7**, 11053 (2016).
- T. Maiyalagan, K. A. Jarvis, S. Therese, P. J. Ferreira, A. Manthiram, Spinel-type lithium cobalt oxide as a bifunctional electrocatalyst for the oxygen evolution and oxygen reduction reactions. *Nat. Commun.* **5**, 3949 (2014).
- P. Rasiyah, A. C. C. Tseung, The role of the lower metal oxide/higher metal oxide couple in oxygen evolution reactions. *J. Electrochem. Soc.* **131**, 803–808 (1984).
- R. Subbaraman *et al.*, Trends in activity for the water electrolyser reactions on 3d $\text{M}(\text{Ni}, \text{Co}, \text{Fe}, \text{Mn})$ hydr(oxy)oxide catalysts. *Nat. Mater.* **11**, 550–557 (2012).
- L. Han, S. Dong, E. Wang, Transition-metal (Co, Ni, and Fe)-based electrocatalysts for the water oxidation reaction. *Adv. Mater.* **28**, 9266–9291 (2016).
- X. Zheng *et al.*, Theory-driven design of high-valence metal sites for water oxidation confirmed using in situ soft X-ray absorption. *Nat. Chem.* **10**, 149–154 (2018).
- Z. Lu *et al.*, Identifying the active surfaces of electrochemically tuned LiCoO_2 for oxygen evolution reaction. *J. Am. Chem. Soc.* **139**, 6270–6276 (2017).
- H. S. Oh *et al.*, Electrochemical catalyst-support effects and their stabilizing role for IrO_x nanoparticle catalysts during the oxygen evolution reaction. *J. Am. Chem. Soc.* **138**, 12552–12563 (2016).
- H. B. Tao *et al.*, Identification of surface reactivity descriptor for transition metal oxides in oxygen evolution reaction. *J. Am. Chem. Soc.* **138**, 9978–9985 (2016).
- D. Yan *et al.*, Defect chemistry of nonprecious-metal electrocatalysts for oxygen reactions. *Adv. Mater.* **29**, 1606459 (2017).
- A. Grimaud *et al.*, Activation of surface oxygen sites on an iridium-based model catalyst for the oxygen evolution reaction. *Nat. Energy* **2**, 16189 (2016).
- F. Song *et al.*, Transition metal oxides as electrocatalysts for the oxygen evolution reaction in alkaline solutions: An application-inspired renaissance. *J. Am. Chem. Soc.* **140**, 7748–7759 (2018).
- Z. Lu *et al.*, Electrochemical tuning of layered lithium transition metal oxides for improvement of oxygen evolution reaction. *Nat. Commun.* **5**, 4345 (2014).
- W. T. Hong *et al.*, Toward the rational design of non-precious transition metal oxides for oxygen electrocatalysis. *Energy Environ. Sci.* **8**, 1404–1427 (2015).
- J. G. Lee *et al.*, A new family of perovskite catalysts for oxygen-evolution reaction in alkaline media: BaNiO_3 and $\text{BaNi}_{0.83}\text{O}_{2.5}$. *J. Am. Chem. Soc.* **138**, 3541–3547 (2016).
- J. R. Petrie *et al.*, Enhanced bifunctional oxygen catalysis in strained LaNiO_3 perovskites. *J. Am. Chem. Soc.* **138**, 2488–2491 (2016).
- E. Fabbri *et al.*, Dynamic surface self-reconstruction is the key of highly active perovskite nano-electrocatalysts for water splitting. *Nat. Mater.* **16**, 925–931 (2017).
- I. Yamada *et al.*, Bifunctional oxygen reaction catalysis of quadruple manganese perovskites. *Adv. Mater.* **29**, 1603004 (2017).
- S. Yagi *et al.*, Covalency-reinforced oxygen evolution reaction catalyst. *Nat. Commun.* **6**, 8249 (2015).
- S. Hirai *et al.*, Non-Fermi liquids as highly active oxygen evolution reaction catalysts. *Adv. Sci. (Weinh.)* **4**, 1700176 (2017).
- R. R. Rao *et al.*, Towards identifying the active sites on RuO_2 (110) in catalyzing oxygen evolution. *Energy Environ. Sci.* **10**, 2626–2637 (2017).
- D. Y. Kuo *et al.*, Influence of surface adsorption on the oxygen evolution reaction on IrO_2 (110). *J. Am. Chem. Soc.* **139**, 3473–3479 (2017).
- Y. T. Kim *et al.*, Balancing activity, stability and conductivity of nanoporous core-shell iridium/iridium oxide oxygen evolution catalysts. *Nat. Commun.* **8**, 1449 (2017).
- T. Bininger *et al.*, Thermodynamic explanation of the universal correlation between oxygen evolution activity and corrosion of oxide catalysts. *Sci. Rep.* **5**, 12167 (2015).
- X. Li *et al.*, Exceptional oxygen evolution reactivities on CaCoO_3 and SrCoO_3 . *Sci. Adv.* **5**, eaav6262 (2019).
- F. Lin *et al.*, Synchrotron X-ray analytical techniques for studying materials electrochemistry in rechargeable batteries. *Chem. Rev.* **117**, 13123–13186 (2017).
- W. Yang *et al.*, Key electronic states in lithium battery materials probed by soft X-ray spectroscopy. *J. Electron Spectrosc. Relat. Phenom.* **190**, 64–74 (2013).
- H. Zhang *et al.*, Developing soft X-ray spectroscopy for in situ characterization of nanocatalysts in catalytic reactions. *J. Electron Spectrosc. Relat. Phenom.* **197**, 118–123 (2014).
- J. Wu *et al.*, Modification of transition-metal redox by interstitial water in hexacyanometalate electrodes for sodium-ion batteries. *J. Am. Chem. Soc.* **139**, 18358–18364 (2017).
- F. De Groot, Multiplet effects in X-ray spectroscopy. *Coord. Chem. Rev.* **249**, 31–63 (2005).
- B. T. Thole, G. van der Laan, Branching ratio in x-ray absorption spectroscopy. *Phys. Rev. B Condens. Matter* **38**, 3158–3171 (1988).
- J. M. Chen *et al.*, A complete high-to-low spin state transition of trivalent cobalt ion in octahedral symmetry in $\text{SrCo}_{0.5}\text{Ru}_{0.5}\text{O}_{3-\delta}$. *J. Am. Chem. Soc.* **136**, 1514–1519 (2014).
- Q. Li *et al.*, Quantitative probe of the transition metal redox in battery electrodes through soft X-ray absorption spectroscopy. *J. Phys. D Appl. Phys.* **49**, 413003 (2016).
- A. J. Achkar *et al.*, Bulk sensitive X-ray absorption spectroscopy free of self-absorption effects. *Phys. Rev. B Condens. Matter Mater. Phys.* **83**, 081106 (2011).
- A. J. Achkar, T. Z. Regier, E. J. Monkman, K. M. Shen, D. G. Hawthorn, Determination of total x-ray absorption coefficient using non-resonant x-ray emission. *Sci. Rep.* **1**, 182 (2011).
- R. Qiao *et al.*, Distinct solid-electrolyte-interphases on Sn (100) and (001) electrodes studied by soft X-ray spectroscopy. *Adv. Mater. Interfaces* **1**, 1300115 (2014).
- S. Sun, H. Li, Z. J. Xu, Impact of surface area in evaluation of catalyst activity. *Joule* **2**, 1024–1027 (2018).
- A. Grimaud *et al.*, Activating lattice oxygen redox reactions in metal oxides to catalyze oxygen evolution. *Nat. Chem.* **9**, 457–465 (2017).
- H. Chou, A. Ismach, R. Ghosh, R. S. Ruoff, A. Dolocan, Revealing the planar chemistry of two-dimensional heterostructures at the atomic level. *Nat. Commun.* **6**, 7482 (2015).
- H. Ji *et al.*, Investigating the origin of $\text{Co}(\text{IV})$'s high electrocatalytic activity in the oxygen evolution reaction at a Na_xCoO_2 interface. *Mater. Res. Bull.* **95**, 285–291 (2017).